



X-Ray Spectroscopy in the Microcalorimeter Era. III. Line Formation under Case A, Case B, Case C, and Case D in H- and He-like Iron for a Photoionized Cloud

P Chakraborty¹ , G. J. Ferland¹ , M. Chatzikos¹ , F. Guzmán² , and Y. Su¹ 

¹ University of Kentucky, Lexington, KY, USA

² University of North Georgia, Dahlonega, GA, USA

Received 2021 February 5; revised 2021 March 6; accepted 2021 March 8; published 2021 April 30

Abstract

Future microcalorimeter X-ray observations will resolve spectral features in unmatched detail. Understanding of line formation processes in X-rays deserves much attention. The purpose of this paper is to discuss such processes in the presence of a photoionizing source. Line formation processes in one- and two-electron species are broadly categorized into four cases. Case A occurs when the Lyman line optical depths are very small and photoexcitation does not occur. Line photons escape the cloud without any scattering. Case B occurs when the Lyman line optical depths are large enough for photons to undergo multiple scatterings. Case C occurs when a broadband continuum source strikes an optically thin cloud. The Lyman lines are enhanced by induced radiative excitation of the atoms/ions by continuum photons, also known as continuum pumping. A fourth, less studied scenario, where the Case B spectrum is enhanced by continuum pumping, is called Case D. Here, we establish the mathematical foundation of Cases A, B, C, and D in an irradiated cloud with Cloudy. We also show the total X-ray emission spectrum for all four cases within the energy range 0.1–10 keV at the resolving power of XRISM around 6 keV. Additionally, we show that the combined effect of electron scattering and partial blockage of continuum pumping reduces the resonance line intensities. Such reduction increases with column density and can serve as an important tool to measure the column density/optical depth of the cloud.

Unified Astronomy Thesaurus concepts: [X-ray astronomy \(1810\)](#); [Photoionization \(2060\)](#)

1. Introduction

Microcalorimeter X-ray missions like Hitomi and the upcoming missions XRISM and Athena will provide unprecedented spectroscopic resolution. The Soft X-Ray Spectrometer (Kelley et al. 2016) on board Hitomi (Hitomi Collaboration et al. 2016) resolved the Fe XXV K α complex in four components for the first time. A plethora of high-resolution X-ray data from these missions will be available within the next few decades. Interpreting these high-resolution spectra requires a clear understanding of the line formation processes in the X-ray emitting plasma.

Line formation in gaseous nebulae was first studied in the 1930s in a series of papers by Menzel (1937), Menzel & Baker (1937), Baker & Menzel (1938), and Baker et al. (1938) for the formation of optical H I lines. Two limiting cases were discussed: “Case A” and “Case B.” Case A occurs when the nebula is optically thin and the line photons emitted by recombination escape the cloud freely. Case B occurs if the nebula is optically thick and the line photons scatter multiple times in the cloud. Higher-order Lyman lines are converted into Balmer and Ly α (or K α) photons or into a two-photon continuum. Note that in their study, the source of the radiation was assumed to be of stellar origin. Stars in the gaseous nebulae might have strong Lyman absorption lines in the spectral energy distribution (SED), and there is almost no continuum pumping. This will be relevant to the discussion later.

A third case occurring in optically thin irradiated clouds, “Case C,” was introduced by Baker et al. (1938) and later followed up by Chamberlain (1953) and Ferland (1999). In Case C, lines escape the cloud freely as in Case A. But unlike Case A, the Case C spectrum is enhanced by continuum pumping.

Some recent studies (Luridiana et al. 2009; Peimbert et al. 2016) have discussed a fourth case, “Case D,” which occurs in

optically thick irradiated systems. Similar to those in Case B, line photons scatter multiple times in Case D before escaping the optically thick cloud. But unlike Case B, the Case D spectrum is enhanced by continuum pumping.

Most of the previous works on Cases A, B, C, and D, both theoretical and observational, focused on the optical, ultraviolet, and infrared regimes (Menzel 1937; Menzel & Baker 1937; Baker & Menzel 1938; Baker et al. 1938; Chamberlain 1953; Soifer et al. 1981; Malkan & Sargent 1982; Hummer & Storey 1987; Keel & Windhorst 1991; Ferland 1999; Sánchez et al. 2007; Stelzer et al. 2012; Mennickent et al. 2016; Peimbert et al. 2017), with a small number of studies on X-rays—Storey & Hummer (1988, 1995) for one-electron ions and Porter & Ferland (2007) for two-electron ions. Some other previous studies on soft X-ray spectra are Paerels & Kahn (2003), Bianchi et al. (2005), Cappi et al. (2006), Guainazzi & Bianchi (2007), and Mao et al. (2018). Note that Kinkhabwala et al. (2002) have outlined many of the physical processes discussed in this paper, focusing on second- and third-row elements.

The purpose of our paper is to describe improvements to the widely disseminated code Cloudy with simultaneous radiative transfer and ionization solutions. This paper presents diagnostic diagrams making it possible to measure column densities from line intensities. Here, we discuss the line formation processes for the four Menzel and Baker cases—Cases A, B, C, and D for H-like and He-like iron in photoionized plasma. This will be essential for interpreting future high-resolution microcalorimeter observations in the presence of a photoionizing source.

This paper is the third in the series “X-Ray Spectroscopy in the Microcalorimeter Era,” the first two papers of which discuss the atomic processes in a collisionally excited plasma. Chakraborty et al. (2020b) discuss line interlocking and resonant Auger destruction (Ross et al. 1978; Band et al. 1990; Ross et al. 1996;

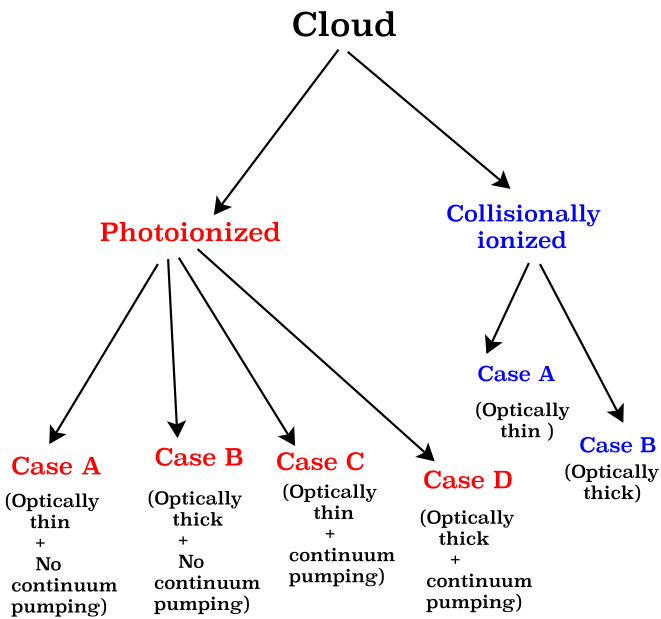


Figure 1. A flowchart showing the line formation conditions occurring in photoionized/collisionally ionized clouds. Case A, Case B, Case C, and Case D occur in photoionized clouds. Case A and Case B also occur in collisionally ionized clouds.

Liedahl 2005) and electron scattering escape (ESE) in the Fe XXV K α complex. Chakraborty et al. (2020c) discuss the Case A to B transition in H- and He-like iron. The present paper explores photoionized X-ray plasma with Cloudy (Ferland et al. 2017) for a power-law SED. Note that the results shown in all three papers of this series apply in the coronal limit, although the formalism will go to equilibrium in high densities. Figures 10–12 in Ferland et al. (2017) display the coronal limit for collisionally ionized and photoionized cases. For iron ($Z = 26$), the coronal limit applies to electron densities lower than 10^{16} cm^{-3} .

The organization of this paper is as follows. Section 2 discusses the theoretical framework of Cases A, B, C, and D. Section 3 lists the simulation parameters used for our calculations. Section 4 describes the results. Section 5 discusses the total emitted spectrum within the energy range 0.1–10 keV. Section 6 describes the effects of background continuum opacities like electron scattering opacity. Section 7 discusses our results. We refer to the transitions going from $n = 2, 3, 4$ to $n = 1$ in H-like iron as Ly α , Ly β , and Ly γ and those in He-like iron as K α , K β , and K γ . Transitions going from $n = 3$ to $n = 2$ are called H α in H-like iron and L α in He-like iron. This nomenclature is inspired by the Siegbahn notation (Siegbahn 1916) as implemented in, for instance, Gabriel (1972), Fukumura & Tsuruta (2004), and Koyama et al. (2007).

2. Theoretical Framework

Lines are formed under Case A, Case B, Case C, or Case D conditions. Case A and Case B occur in collisionally ionized clouds. Case A, Case B, Case C, and Case D occur in photoionized clouds. Figure 1 shows the four cases for the two ionizing conditions. Line formation processes in collisionally ionized clouds have been discussed in the first two papers of this series. This paper solely focuses on photoionized clouds.

A schematic representation of all four cases is shown in Figure 2 for a simplified three-level system. Low-column-

density (optically thin) regions can be described by Case A or Case C depending on the ionizing radiation. In both cases, line photons escape the cloud without any scattering. Case A occurs when the continuum radiation hitting the cloud has strong absorption features in the Lyman lines. There is no continuum pumping in the Lyman lines emitted by the cloud. Lines in the Case A limit are solely formed by radiative recombination and cascades from higher levels.³ Case C occurs if the continuum source striking the optically thin cloud does not contain Lyman absorption lines and the emitted Lyman lines are enhanced by continuum pumping. As a result, the Case C spectrum is always brighter than Case A.

The ratio of the Case C to the Case A line intensities can be calculated from the ratio of the continuum pumping rate to the rate of recombination (r). In equilibrium, r is equal to the rate of photoionization (Γ_n):

$$\Gamma_n = \int_{\nu_0}^{\infty} \frac{4\pi J_{\nu}}{h\nu} \alpha_{\nu} d\nu \quad (\text{s}^{-1}) \quad (1)$$

where J_{ν} (erg cm $^{-2}$ s $^{-1}$ sr $^{-1}$ Hz $^{-1}$) is the mean intensity per unit frequency per unit solid angle of the incident radiation and α_{ν} is the photoionization cross section (cm 2) for the atom/ion by photons of energy $h\nu$.

The rate of continuum pumping of a line from level l to level u is given by

$$\Gamma_l = B_{lu} J_l = f_{lu} \frac{\pi e^2}{mc} \left(\frac{4\pi J_l}{h\nu} \right) \quad (\text{s}^{-1}) \quad (2)$$

where B_{lu} is the Einstein coefficient, f_{lu} is the oscillator strength, and the other symbols have their usual meanings.

For a power-law ($f_{\nu} \propto \nu^{-1}$) model in H-like iron for the Ly α transition in a simple two-level system,

$$\frac{\Gamma_l}{r} \sim 16. \quad (3)$$

This implies that Ly α line intensities are ~ 16 times enhanced in Case C as compared to Case A. The calculated ratio is approximate, as the real calculation will have many pumping lines and many different branching ratios. This ratio is approximately in agreement with the line intensities listed in Table 1 obtained from our Cloudy simulations, which shows that the Case C Ly α in H-like iron is ~ 10 times enhanced as compared to Case A.

In contrast, Case B occurs in the high-column-density limit ($N_H \geq 10^{21.5} \text{ cm}^{-2}$). In this limit, Lyman line optical depths are large enough for photons to undergo multiple scatterings and so are converted into H α (or L α) and Ly α (or K α) photons or into a two-photon continuum. The cloud becomes self-shielding, stopping the continuum pumping despite the presence of a continuum radiation source in the cloud. Typically, Case B describes the line formation in most observed optically thick nebulae (Osterbrock & Ferland 2006).

Case D occurs if Lyman line optical depths are large but the cloud does not entirely become self-shielding to the external radiation. Luridiana et al. (2009) argued that a real nebula in the optically thick limit would be better represented by Case D than by Case B. Their study reported a significant contribution of continuum pumping to Balmer emissivity in the H II region. As

³ As described in Chakraborty et al. (2020c), in a collisionally ionized cloud in the absence of photoionizing radiation, line formation in the optically thin limit is also described by Case A.

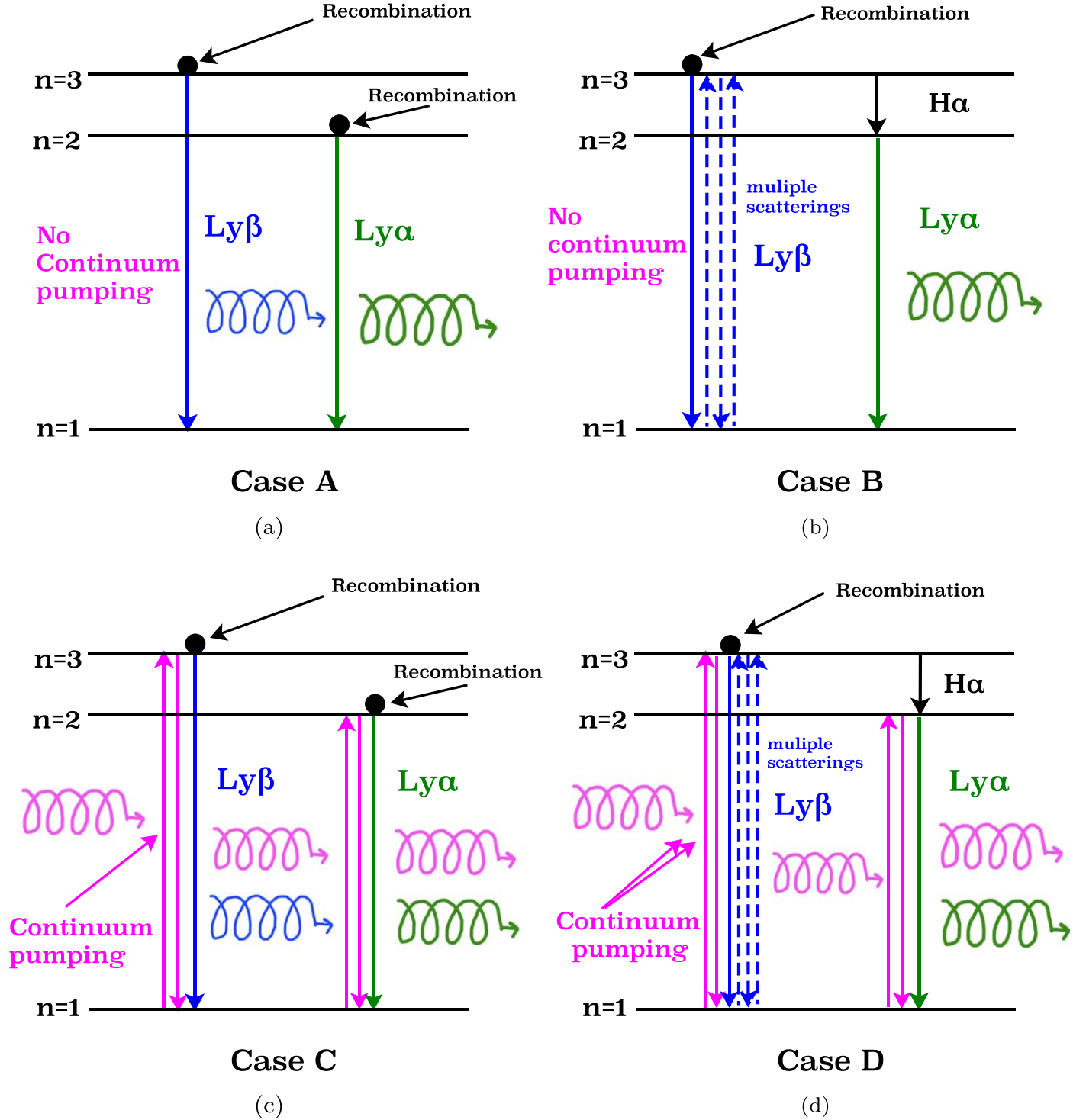


Figure 2. A simplified three-level representation of Case A, Case B, Case C, and Case D shown for an H-like system. The same atomic processes occur in He-like systems too. The top-left panel shows Case A, where the lines are formed by radiative recombination and cascades from higher levels. There is no continuum pumping. The cloud is optically thin, and all Lyman photons escape the cloud without scattering/absorption. The top-right panel shows Case B, where the cloud is optically thick and continuum pumping photons are blocked. Higher- n Lyman photons (Ly β in the diagram) scatter multiple times to generate Balmer (here H α) and Ly α photons. The bottom-left panel shows Case C, where in addition to radiative recombination and downward cascades, Lyman lines are also enhanced by continuum pumping. The enhanced Lyman lines escape the optically thin cloud. The bottom-right panel shows Case D, where multiple scatterings and continuum pumping in Lyman lines occur together in an optically thick cloud. The two-photon continuum is not shown because it does not make emission lines.

far as we know, Case D has not been studied in the X-ray to date. Our calculations for the X-ray regime in the optically thick limit show substantial enhancement in the Lyman and Balmer line intensities in H- and He-like iron. This will be further elaborated in Section 4.4.

3. Simulation Parameters

This section discusses the simulation parameters used in Cloudy. We aim to establish a standard mathematical framework of line formation through Case A, Case B, Case C, and

Table 1
Line Intensities per Unit Thickness (I/d) for Case A, B, C, and D Conditions for Certain Lyman and Balmer Transitions in H- and He-like Ions in a Photoionized Cloud

Ion	Transitions	Wavelength	I/d (erg cm $^{-3}$ s $^{-1}$)				
			Case A	Case B _{classic}	Case B	Case C	Case D
H-like	$2^2P \rightarrow 1^2S$	1.77982 Å	6.22e-25	8.24e-25	3.05e-25	6.05e-24	4.15e-25
	$3^2P \rightarrow 1^2S$	1.50273 Å	1.43e-25	2.84e-26	1.57e-26	9.06e-25	2.69e-26
	$3^2P \rightarrow 2^2S$	9.65247 Å	4.99e-26	8.94e-26	4.89e-26	7.17e-26	6.68e-26
	$4^2P \rightarrow 1^2S$	1.42505 Å	5.55e-26	1.05e-26	9.67e-27	3.07e-25	1.89e-26
	$4^2P \rightarrow 2^2S$	7.14920 Å	1.86e-26	3.09e-26	1.69e-26	2.71e-26	2.05e-26
He-like	$2^1P \rightarrow 1^1S(w)$	1.85040 Å	1.69e-25	1.74e-25	1.29e-25	4.35e-24	2.69e-25
	$2^3P_2 \rightarrow 1^1S(x)$	1.85541 Å	2.41e-25	2.46e-25	1.85e-25	2.59e-25	2.02e-25
	$2^3P_1 \rightarrow 1^1S(y)$	1.85951 Å	1.82e-25	1.89e-25	1.59e-25	5.77e-25	1.97e-25
	$2^3S \rightarrow 1^1S(z)$	1.86819 Å	2.68e-25	3.72e-25	4.23e-25	4.12e-25	4.83e-25
	$3^1P \rightarrow 1^1S$	1.57317 Å	4.53e-26	1.36e-26	8.89e-27	7.32e-25	2.74e-26
	$3^3P \rightarrow 1^1S$	1.57456 Å	9.81e-26	1.45e-26	1.23e-26	3.09e-25	1.68e-26
	$3^1P \rightarrow 2^1S$	10.2202 Å	4.41e-28	5.53e-27	5.41e-27	7.14e-27	9.72e-27
	$3^3P \rightarrow 2^3S$	10.0178 Å	6.96e-27	1.91e-26	1.87e-26	2.19e-26	2.82e-26
	$4^1P \rightarrow 1^1S$	1.49460 Å	1.82e-26	8.28e-27	5.37e-27	2.51e-25	1.92e-26
	$4^3P \rightarrow 1^1S$	1.49513 Å	3.61e-26	9.36e-27	7.77e-27	1.06e-25	1.19e-26
	$4^1P \rightarrow 2^1S$	7.61825 Å	2.40e-28	1.73e-27	1.68e-27	3.32e-27	3.77e-27
	$4^3P \rightarrow 2^3S$	7.48713 Å	3.24e-27	6.91e-27	6.78e-27	9.54e-27	1.11e-26

Notes. The I/d for Cases A and C are listed for $N_{\text{H}} = 10^{19}$ cm $^{-2}$, and those for Cases B and D are listed for $N_{\text{H}} = 10^{24}$ cm $^{-2}$. The I/d listed under Case A, Case B, Case C, and Case D are what will be observed in nature. Case B_{classic}, the classic Menzel–Baker Case B, has also been included in the table for educational purposes.

Case D. The simulation parameters have been chosen accordingly. All the simulations are done using the development version of Cloudy with a hydrogen density of 1 cm $^{-3}$. To make the simplest case, the shape of the incident radiation field is assumed to be a power-law SED:

$$f_{\nu} \propto \nu^{-\alpha} \quad (4)$$

with $\alpha = 1$.

The intensity of the radiation field is characterized by the ionization parameter (U), defined with the following ratio:

$$U = \frac{\Phi_{\text{H}}}{n_{\text{H}} c} \quad (5)$$

where Φ_{H} is the flux of hydrogen-ionizing photons, n_{H} is the hydrogen density, and c is the speed of light.

Much of the X-ray literature uses the ξ ionization parameter defined by Kallman & Bautista (2001). For our $\alpha = 1$ SED, $\xi = 1$ corresponds to a U of 0.01767.

Figure 3 shows the variation of different ionization stages in iron with the log of U . The top x -axis shows the log of ξ . The left panel of the figure shows a linear plot, and the right panel shows a log plot. We choose $\log U = 2$ ($\log \xi = 3.75$) to maximize the quantity of H- and He-like iron in the cloud. This also minimizes the overlap between He- and Li-like iron ions, as Li-like iron selectively changes the He-like spectra by line interlocking (Chakraborty et al. 2020b). The linear figure also shows our choice of ionization parameter with a black vertical line. Note that our choice of ionization parameter is in agreement with the range of ξ for highly charged iron mentioned in Kallman et al. (2004; $\log \xi \geq 2$), who also discussed K lines in iron in a photoionized cloud for a power-law SED.

The cloud temperature (T) is obtained from the energy equilibrium equation from a heating–cooling balance to replicate the actual physical temperature of a photoionized

cloud. The computed temperature is $T \sim 6 \times 10^6$ K at $\log U = 2$. The variation of T with $\log U$ is shown in Figure 4. Note that photoionized clouds are a lot cooler than collisionally ionized clouds. In fact, this equilibrium temperature is about 8 times smaller than that of the collisionally ionized plasma considered in the first two papers of this series.

4. Results

This section explores different conditions for lines to form in the presence of a photoionizing source emitting in X-rays. Table 1 shows a comparison between selected line intensities (including the K α complex) for Case A, Case B, Case C, and Case D conditions for H- and He-like iron. The quantity listed in the table is the line intensity (I) per unit thickness (d), I/d . As the line intensities increase as the cloud’s size/thickness increases, I/d tracks the scaled change in the line intensities for all four cases or the transition between them. Although I/d has the same units as the emissivity of a line, $4\pi j$, it does not have the same physical interpretation. All the I/d listed in Table 1 are observed in nature except for Case B_{classic}, which will be further discussed in Section 4.2. The line wavelengths listed in the table are taken from the National Institute of Standards and Technology⁴ (version 5.8; Kramida et al. 2018).

The low-column-density (optically thin) limit represents Cases A and C, and the high-column-density (optically thick) limit represents Cases B and D. Therefore, the I/d listed in the table for Cases A and C are computed at $N_{\text{H}} = 10^{19}$ cm $^{-2}$ and those for Cases B and D at $N_{\text{H}} = 10^{24}$ cm $^{-2}$. The continuous variation of I/d with hydrogen column density and the transition from Case A to B and Case C to D are shown in Figure 5.

⁴ <https://physics.nist.gov/asd>

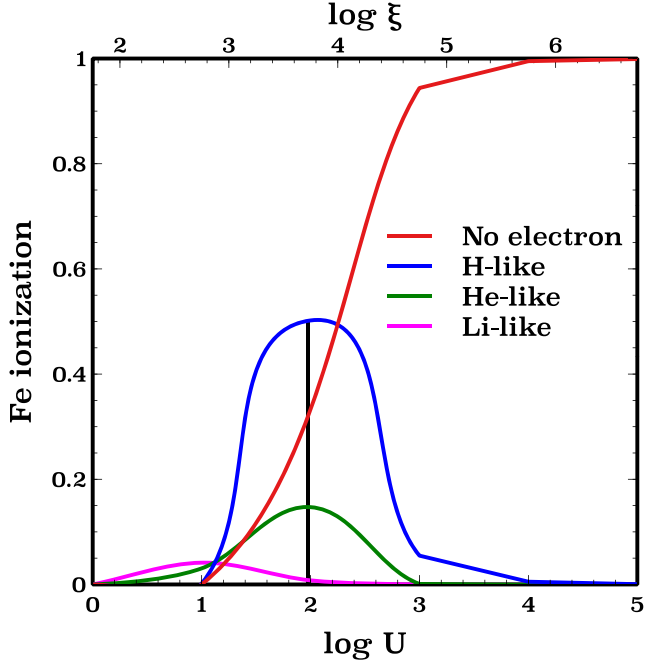


Figure 3. Ionization in iron vs. log of ionization parameter (U). The left and right panels show the iron ionization in linear and log scales. Red, blue, green, and magenta lines show the fraction of no-electron, H-like, He-like, and Li-like iron. A vertical black line is drawn at $\log U = 2$ in the linear plot, the ionization parameter chosen for our calculations. The x-axes at the top in both figures show $\log \xi$.

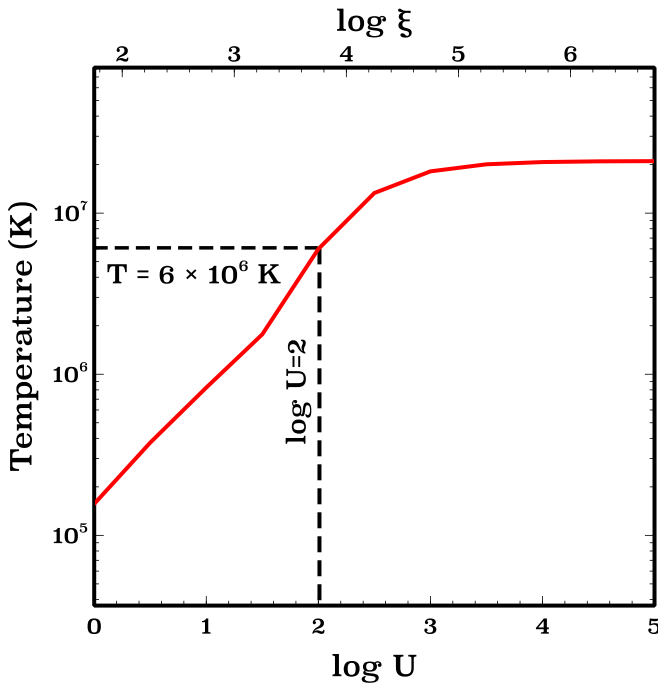
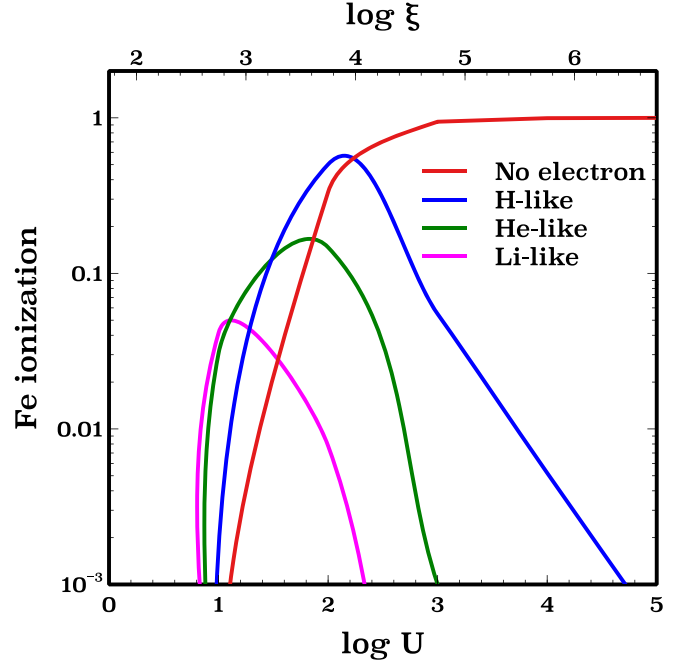


Figure 4. Temperature of the photoionized cloud vs. log of ionization parameter ($\log U$) for a 1 cm^3 plasma. The black dashed lines show the temperature at our choice of ionization parameter, $\log U = 2$. The x-axis at the top shows $\log \xi$.

4.1. Case A

A schematic representation of Case A is shown in the upper-left panel of Figure 2. Case A is the simplest of all four cases occurring in optically thin systems. As mentioned in the introduction, Case A was developed for SEDs with strong Lyman absorption features—for example, stellar SEDs. The strong Lyman absorption lines in the SED prevent continuum pumping. The continuum pumping in our simulated cloud is stopped using the Cloudy command



no induced processes.

The top panel of Figure 5 shows that I/d in H- and He-like iron remains constant up to $N_{\text{H}} = \sim 10^{21.5} \text{ cm}^{-2}$. This is because up to this column density, Lyman lines escape without any scattering/absorption, and any column density lower than $N_{\text{H}} = 10^{21.5} \text{ cm}^{-2}$ will generate a pure Case A spectrum. Table 1 shows the I/d for Case A at $N_{\text{H}} = 10^{19} \text{ cm}^{-2}$.

4.2. Case B

The top-right panel of Figure 2 shows the Case B condition in a cloud. Continuum pumping is disabled as in Section 4.1. As shown in Figure 5, column densities higher than $N_{\text{H}} \sim 10^{21.5} \text{ cm}^{-2}$ begin to make a transition to the Case B limit. Two types of Case B are shown—Case B_{classic} and Case B. The dashed and solid lines in the top panel of Figure 5 represent Case B_{classic} and Case B, respectively. What we refer to as Case B throughout the text considers all the physical processes observed in nature in the X-ray limit, including electron scattering and line overlap. The concept of electron scattering is described later in this section and in Section 6. Case B_{classic} is the Menzel–Baker Case B values studied in the 1930s, which do not include electron scattering or line overlap. In Cloudy, electron scattering can be disabled with the following command:

no electron scattering.

We find that for X-ray emission from H- and He-like iron, Case B_{classic} remains a pedagogical scenario.

Table 1 shows the I/d values for Case B_{classic} and Case B (observed in nature) at $N_{\text{H}} = 10^{24} \text{ cm}^{-2}$. In the typical Menzel–Baker Case B_{classic}, as a consequence of the conversion of higher- n Lyman lines into Ly α (or K α) and Balmer lines, Ly α (or K α) intensity increases, Ly β (or K β) and higher- n Lyman line intensities decrease, and H α (or L α) and higher-order Balmer line intensities increase as compared to the Case A limit. The Case B_{classic} column in the table exactly reflects this behavior for both H- and He-like iron. For instance in H-like

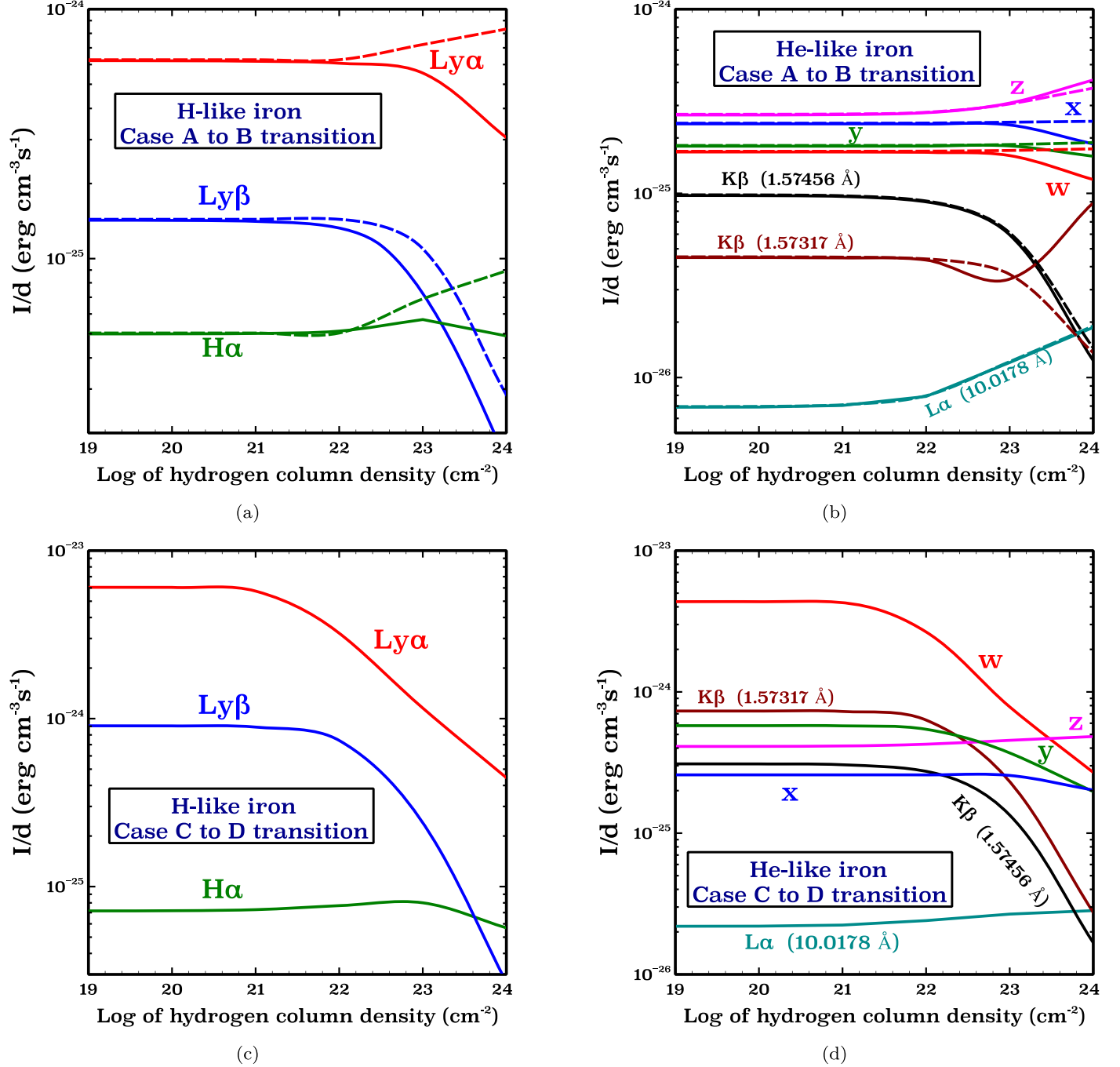


Figure 5. Line intensity per unit thickness of the cloud vs. the log of hydrogen column density. The figures in the top panel show the Case A to Case B transition in H- and He-like iron. Dashed lines represent the classic Menzel–Baker Case A to Case B limit, and solid lines represent the observed Case A to Case B limit. The figures in the bottom panel show the observed Case C to Case D transition in H- and He-like iron.

iron, I/d in $\text{Ly}\alpha$ increases by $\sim 32\%$, $\text{Ly}\beta$ decreases by $\sim 80\%$, and $\text{H}\alpha$ increases by $\sim 80\%$ at $N_{\text{H}} = 10^{24} \text{ cm}^{-2}$. In He-like iron, I/d in z increases by $\sim 40\%$, x , y , and w increase very slightly ($\leq 4\%$), $\text{K}\beta$ decreases by $\sim 3\text{--}7$ times, and $\text{L}\alpha$ increases by $\sim 3\text{--}13$ times as compared to Case A.

However, the observed Case B values are quite different from the Case B_{classic} values. In fact, in H-like iron, all Lyman I/d values decrease as compared to the Case A limit, including $\text{Ly}\alpha$. H-like $\text{Ly}\alpha$ decreases by $\sim 50\%$. In He-like iron, selected $\text{K}\alpha$ lines (x , y , and w) show a decrease up to $\sim 24\%$.

Such a decrease in the line intensities in the observed Case B mainly occurs due to electron scattering, as described in

Section 6. When line photons scatter off high-speed electrons, they are largely Doppler-shifted from their line-center. Lines with the largest optical depths are more likely to exhibit a reduction in their line intensities as they are more likely to scatter. Figure 6 shows the optical depth of certain Lyman and Balmer lines in H- and He-like iron. In H-like iron, $\text{Ly}\alpha$, $\text{Ly}\beta$, and $\text{Ly}\gamma$ intensities are reduced due to electron scattering because of their large optical depths. In He-like iron, w , y , $\text{K}\beta$, and $\text{K}\gamma$ intensities are reduced. The optical depth in z is negligible at $N_{\text{H}} = 10^{24} \text{ cm}^{-2}$, and thus I/d for z is not affected by electron scattering. The reduction in I/d for x is due not to electron scattering but to a series of processes described in the

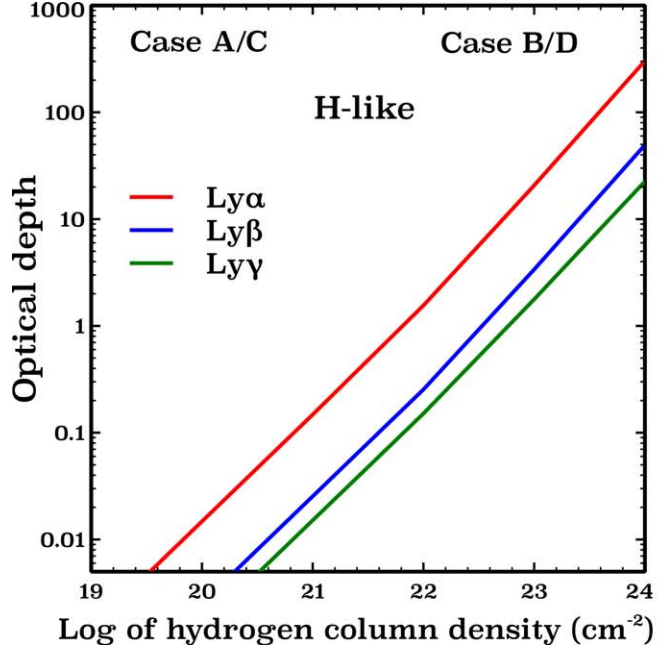


Figure 6. Optical depth vs. log of hydrogen column density for important Ly α , Ly β , and Ly γ transitions in H-like iron and for K α , K β , and K γ transitions in He-like iron. The low-column-density limit represents Case A or Case C. The high-column-density limit represents Case B or Case D.

appendix of Chakraborty et al. (2020b). This explains the observed Case B behavior in both Table 1 and Figure 5.

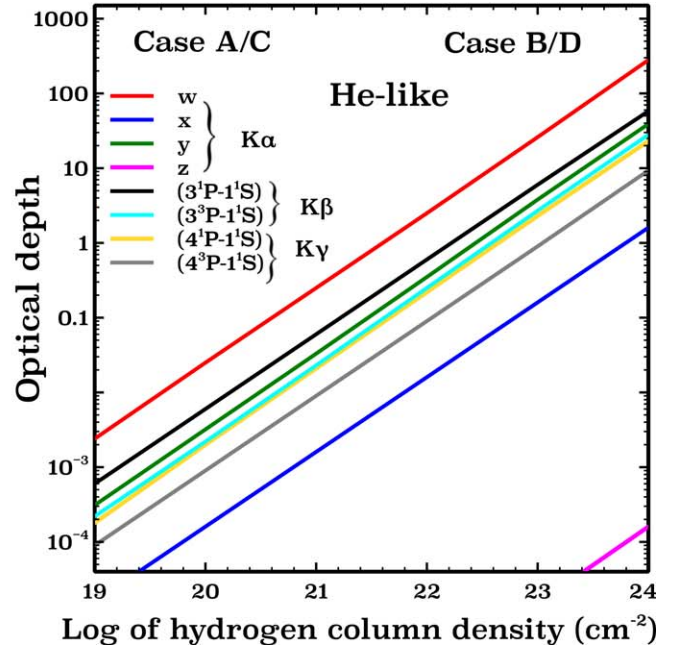
4.3. Case C

The bottom-left panel of Figure 2 represents the Case C condition in a photoionized cloud. Case C occurs in optically thin clouds, like Case A. However, the Case C spectrum is enhanced by the continuum pumping/fluorescence and is the brightest spectrum of all four cases. This can be seen in Table 1 and in the bottom panel of Figure 5. The degree of enhancement depends on the shape of the incident radiation field (Ferland 1999). In our case, a power-law SED fluoresces the cloud (refer to Section 3 for details).

The enhancement in the I/d values in Case C is measured with respect to the Case A spectrum. From the Cloudy simulation listed in Table 1, we find that the I/d for Case C for the Ly α transition for H-like iron gets ~ 10 times amplified as compared to that of Case A. This approximately agrees with the theoretical value of amplification shown in Section 2. Both Ly β and Ly γ lines get amplified by ~ 6 times. Further, our calculation for He-like iron shows that w is enhanced by ~ 27 times, and x , y , and z are enhanced by ~ 1.1 , 3.2 , and 1.5 times, respectively. The K β and K γ transitions are enhanced by ~ 3 – 16 times and ~ 3 – 14 times, respectively. The Balmer lines are enhanced by up to ~ 16 times.

4.4. Case D

The Case D condition in the cloud is shown in the bottom-right panel of Figure 3, where continuum pumping and multiple scatterings happen together. The cloud is partially self-shielded, and lines are partially enhanced by incident radiation. Case D has been hardly discussed in the literature, as at very high column densities, a cloud can become entirely self-shielded, and there is essentially no Case D. The spectral behavior is described by Case B in such cases.



Case D becomes useful when the cloud's column density is high enough to allow multiple scatterings but cannot entirely stop the continuum radiation from penetrating the cloud. In fact, we find that for X-ray emission from H- and He-like plasma, Case D deviates considerably from Case B even at a column density as high as $N_H = 10^{24} \text{ cm}^{-2}$. As shown in Table 1 at $N_H = 10^{24} \text{ cm}^{-2}$, the observed Case D value of I/d for H-like iron is $\sim 36\%$ enhanced in Ly α , $\sim 71\%$ enhanced in Ly β , and $\sim 37\%$ enhanced in H α as compared to the observed Case B value. In He-like iron, w , x , y , and z are enhanced by $\sim 109\%$, $\sim 9\%$, $\sim 24\%$, and $\sim 14\%$, respectively. K β is enhanced by $\sim 208\%$ (for $3^1P \rightarrow 1^1S$) and $\sim 37\%$ (for $3^3P \rightarrow 1^1S$). K α is enhanced by $\sim 80\%$ (for $3^1P \rightarrow 2^1S$) and $\sim 51\%$ (for $3^3P \rightarrow 2^3S$).

Future microcalorimeters will detect ever-so-slight changes in the spectra, thanks to their unmatched spectral resolution. Thus it becomes crucial to understand Case D behavior in optically thick irradiated clouds and its deviation from Case B, especially for column densities $N_H \leq 10^{24} \text{ cm}^{-2}$. Needless to say, at even higher column densities, where the optical depth becomes very large, external radiation will be completely absorbed in the gas. Case D values will eventually approach the Case B values. But until the cloud is thick enough to stop continuum pumping entirely, Case D will be the best description of the emission spectra in irradiated clouds.

4.5. Case A/Case C to Case B/Case D Transition

What drives the Case A to Case B or Case C to Case D transition in a real astronomical scenario is the variation in column density from the low-column-density (optically thin) to the high-column-density (optically thick) limit. Figure 5 shows these transitions for H-like and He-like iron in a photoionized cloud.

When Cases A and B were first discussed in the 1930s, the source of the radiation was assumed to be stellar with strong Lyman absorption lines and no continuum pumping. Thus, galactic nebulae with strong absorption features show the Case A to Case B transition under the variation in column density.

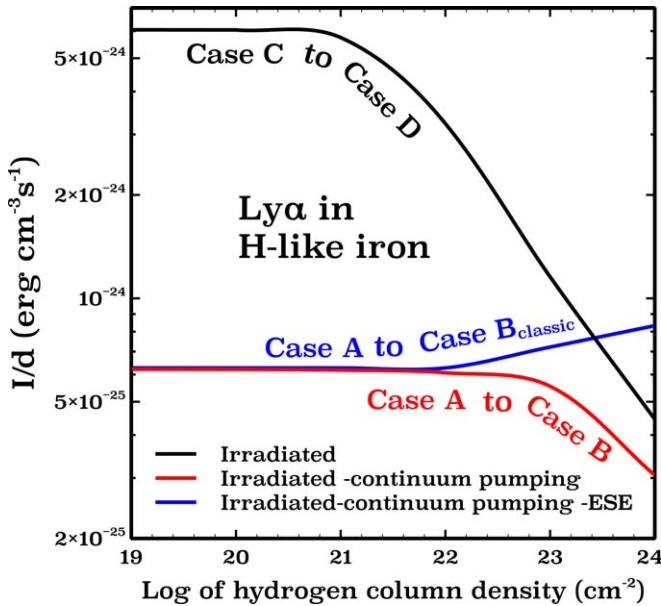


Figure 7. Case C to D, Case A to B, and Case A to B_{classic} transitions shown in the same figure for an irradiated cloud in Ly α for H-like iron. The three curves shown in this figure are plotted separately in the left panel of Figure 5 along with other lines. The Case C to D transition curve includes continuum pumping and electron scattering. The Case A to B transition curve includes electron scattering but not continuum pumping. The Case A to B_{classic} transition curve does not include continuum pumping or electron scattering and is the simplest of all three cases.

The Case A to Case B transition also occurs in any collisionally ionized cloud, as discussed in the first two papers of this series (Chakraborty et al. 2020b, 2020c). Chakraborty et al. (2020c) showed that the Fe XXV K α line ratios calculated with Cloudy are in excellent agreement with the line ratios observed by Hitomi (Hitomi Collaboration et al. 2016) for the outer region of the Perseus core (see Figure 14 in their paper). At the best-fit hydrogen column density of the hot gas at the Perseus core ($N_{\text{H,hot}} = 1.88 \times 10^{21} \text{ cm}^{-2}$) reported by Hitomi Collaboration et al. (2018a), line formation processes can be best described by Case A.

In extragalactic environments, such as a cloud photoionized by an active galactic nucleus (AGN) SED with no Lyman absorption lines, the line formation in the low-column-density limit will be described by Case C in the optically thin limit and by Case D in the optically thick limit until the cloud becomes very optically thick to stop continuum pumping.

Figure 7 shows the variation of I/d in H-like iron with the hydrogen column density for the most complex system observed in nature (the Case C to D transition) to the simplest possible system (the Case A to B_{classic} transition). The Case C to B transition shows the observed I/d values in an irradiated cloud, which includes continuum pumping and electron scattering. The Case A to B transition shows the observed I/d with no continuum pumping. Case A to B_{classic} shows the classic Menzel–Baker transition with no continuum pumping and no electron scattering.

5. Description of Spectral Features

Figure 8 shows the total observed X-ray spectrum coming from a photoionized cloud for Cases A, B, C, and D within the energy range 0.1–10 keV. The spectrum is generated at the resolving power of XRISM ($R \sim 1200$) at 6 keV set to Cloudy.

Similar to that in Section 4, the y-axis of the figure has been scaled to show the total emission (νF_ν) per unit thickness (d) of the cloud, $\nu F_\nu/d$. νF_ν is the sum of the total continuum emission and discrete line intensity (I) multiplied by R :

$$\nu F_\nu = \nu F_\nu^{\text{continuum}} + RI. \quad (6)$$

In Cloudy, νF_ν can be stored with the command `save emitted continuum` added to the input script.

The top and bottom rows in Figure 8 overplot the total emission spectrum for Case A with Case C and that for Case B with Case D. The column densities set to the cloud for calculating the spectra are the same as those in Section 4. The left and right panels show the same plots in linear and log scale, respectively. Clearly, Case C is enhanced as compared to the Case A spectrum due to continuum pumping. Case D is also brighter than Case B due to partial continuum pumping.

Figure 9 shows a simplified plot for a hydrogen-and-iron-only model under Case D conditions. This is not what is observed in nature. The purpose of this figure is to present the components of the spectra coming from H- and He-like iron in a less complicated form. The Lyman and Balmer lines are marked black, and the ionization edges of H-like and He-like iron at ~ 9.3 keV and ~ 8.8 keV are marked blue.

6. Additional Factors Changing the Line Intensities

The background continuum opacity of the photoionized cloud consists of two types of opacities—absorption opacity and scattering opacity. Figure 10 shows these two types of opacities. Absorption opacity mostly comes from the photoelectric absorption/photoionization opacity.⁵ Near the K α complex, absorption opacity is many orders of magnitude smaller than the scattering opacity, making it unimportant without affecting the line spectrum. Thus we only discuss the effects of scattering opacity.

Scattering opacity mostly comes from the scattering of line photons by high-speed thermal electrons that leads to a process called ESE. The concept of ESE has been elaborated in Section 7 of the first paper of this series (Chakraborty et al. 2020b).

As a result of scattering off high-speed electrons, a fraction of the line photons are largely Doppler-shifted from their line-center. These Doppler-shifted photons create super-broad Gaussian profiles. The observed spectrum will include these broad Gaussian profiles as well as the actual sharp line profiles for the fraction of photons that were not scattered (Miller et al. 2002; Hanke et al. 2009).

In Cloudy, these broad Gaussian profiles can be excluded with the following Cloudy command:⁶

```
no scattering intensity,  
reporting only the intensities of the sharp line profiles.
```

Figure 11 shows the total scaled emission near the Fe XXV K α complex. For simplicity, the widths of the sharp line profiles are assumed to be coming from the thermal velocity of the iron ions only. The presence of turbulence will change the widths of the sharp components, but the physics of electron scattering will be the same. At $T = 6 \times 10^6$ K, the temperature

⁵ Other absorption opacities like Brems opacity and dust opacity are negligible as Brems opacity depends on the density square, which is very small (1 cm^{-3}), and we assume no dust is present in our model.

⁶ This is a new Cloudy command that counts the intensity of the remaining line photons that did not suffer electron scattering. The next update to the release version of Cloudy, C17.03, will include this command.

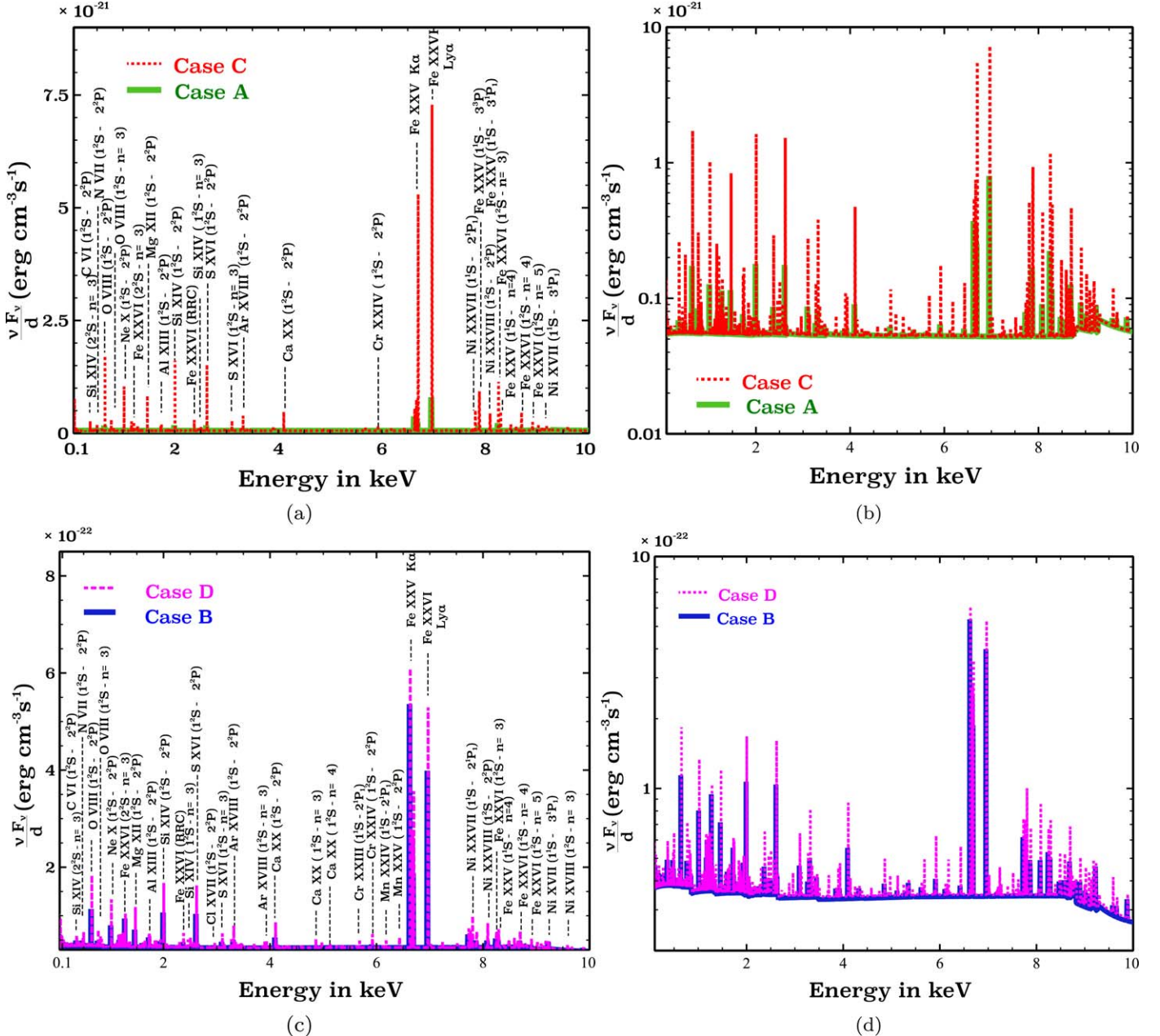


Figure 8. The total scaled emission spectrum for Case A, B, C, and D conditions within the energy range 0.1–10 keV at the resolving power of XRISM ($R \sim 1200$) around 6 keV. The top-left and top-right panels show the Case A (green) and Case C (red) spectra in linear and log scale. The bottom-left and bottom-right panels show the Case B (blue) and Case D (magenta) spectra in linear and log scale. Case C is brighter than Case A due to continuum pumping, and Case D is brighter than Case B due to partial continuum pumping.

of our simulated cloud, the FWHMs of these sharp line profiles at $E \sim 6.7$ keV are $\Delta E_{\text{FWHM}}^{\text{sharp}} = 2\sqrt{\ln 2} \frac{u_{\text{Dop}}}{c} E \sim 1.6$ eV, where $u_{\text{Dop}} = \sqrt{\frac{2kT}{m_{\text{Fe}}}} \sim 43$ km s⁻¹. At the same temperature, the FWHMs of the broad line profiles are $\Delta E_{\text{FWHM}}^{\text{broad}} \sim 0.5$ keV, where $u_{\text{Dop}} = \sqrt{\frac{2kT}{m_e}} \sim 13,500$ km s⁻¹. This implies that the height of broad Gaussians will be orders of magnitude smaller than the sharp components and will be difficult to detect by telescope (Torrejón et al. 2010).

The left panel in Figure 11 shows the changes in the total scaled emission in log scale for the hydrogen column densities $N_{\text{H}} = 10^{20}$, 10^{22} , and 10^{24} cm⁻² in the presence of continuum pumping. The broad Gaussians shown in the figure are solely

from the electron scattering of the photons in the Fe XXV K α complex. We do not show the broad Gaussians from the other lines to keep the figure simple.

The right panel shows a zoomed-in version of the sharp line profiles for all three column densities on a linear scale. As continuum pumping is present, $\nu F_{\nu}/d$ at $N_{\text{H}} = 10^{20}$ cm⁻² represents the Case C limit, and $N_{\text{H}} = 10^{24}$ cm⁻² represents the Case D limit.

It can be seen from the figure that the w line intensity reduces significantly with the increase in optical depth/column density. There are two factors responsible for this reduction. First, the continuum pumping begins to become partially blocked with the increase in optical depth. Second, w has the largest line optical depth among all He-like transitions and is more likely to

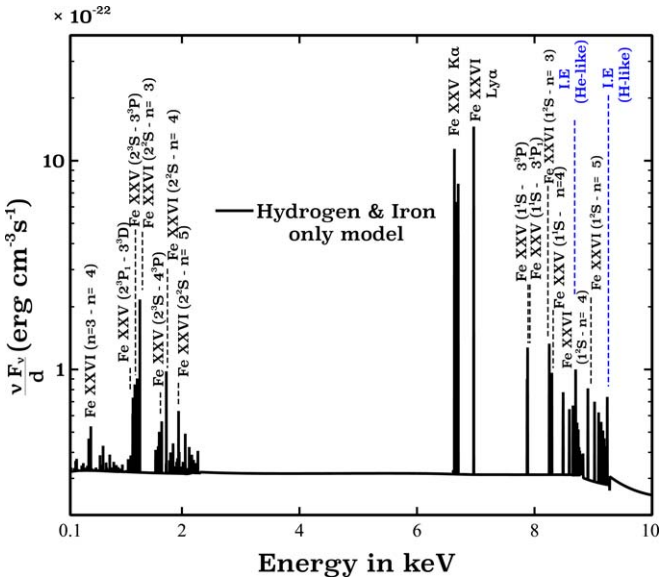


Figure 9. A pedagogical simplified Case D spectrum for a hydrogen-and-iron-only model. Lyman and Balmer lines in H- and He-like iron are marked with black dashed lines. Ionization edges for H- and He-like iron are shown with blue dashed lines.

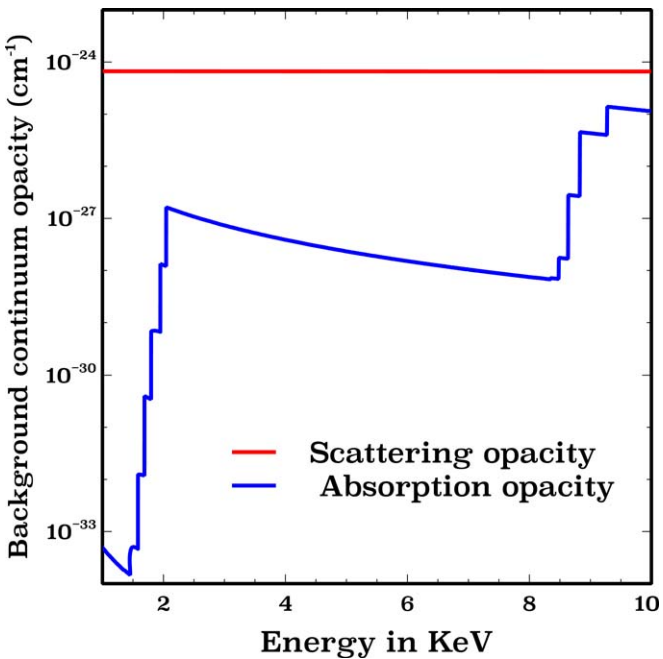


Figure 10. Continuum background opacities in a photoionized iron-and-hydrogen-only model. The red solid line shows the total scattering opacity. The blue line shows the total absorption opacity.

suffer electron scattering. Of course, when observed by future high-resolution telescopes like XRISM and Athena, the electron-scattered broad Gaussian component of w will be much fainter than the sharp component. But the reduction in the sharp w line intensity (or the line intensity of any resonance line) with increasing optical depth can serve as a powerful optical depth/column density diagnostic.

Note that Gilfanov et al. (1987) have discussed the effects of resonance scattering and shown distortion in the radial surface brightness profile due to migration of resonance X-ray line photons from the cluster center to the outer region. This will

lead to a suppression of line fluxes in the central region of a cluster. For example, in Perseus, this factor was reported to be ~ 1.3 for w ($\tau \sim 1$) near the cluster center by Hitomi Collaboration et al. (2018b). Of course, the suppression factor will be different in other systems depending on the geometry and optical depth.

The calculations presented in this paper represent a general study for a photoionized system irradiated with a power-law SED. From our Cloudy calculation, the suppression in w line intensity at $\tau = 1$ is ~ 1.43 due to the joint contribution of partial continuum pumping and electron scattering. Therefore it is safe to say that the change in the resonance line intensities due to these two factors can be as important as the resonance scattering effects. Our current model predicts the total emission from a symmetric geometry, so scattering has no effect on the emergent intensity. In addition to what we report in this paper, the Gilfanov et al. (1987) resonance scattering geometric correction has to be applied to match the observed spectra.

7. Discussion and Conclusion

1. Line formation processes were broadly categorized into two cases in the 1930s—Case A and Case B (Menzel 1937; Menzel & Baker 1937; Baker & Menzel 1938; Baker et al. 1938). At that time, the SED ionizing the cloud was assumed to have strong Lyman absorption lines. There was no continuum pumping/fluorescence to enhance the spectra. Some examples are O-stars in starburst galaxies, planetary nebulae, etc. (Osterbrock & Ferland 2006). But in extragalactic environments such as a cloud photoionized by an AGN SED or galaxies with quasars with no Lyman absorption lines, continuum pumping will significantly enhance the spectra. This led to the discovery of a third case in the late 1930s—Case C (Baker et al. 1938), which describes optically thin clouds in the presence of continuum pumping. A fourth case, Case D, was discovered recently (Luridiana et al. 2009), which describes spectra from an optically thick cloud in the presence of continuum pumping.
2. Figure 3 shows a schematic representation of all four cases.
 - (a) Under Case A conditions, lines are formed by radiative recombination and cascades from higher levels. Lyman lines escape the optically thin cloud without scattering/absorption.
 - (b) Case B occurs when higher- n Lyman lines are converted to Balmer lines and a Ly α (or K α) or two-photon continuum due to multiple scatterings in an optically thick cloud.
 - (c) Lines are formed under Case C when Lyman lines are enhanced by continuum pumping and freely escape the optically thin cloud.
 - (d) Case D occurs when multiple scattering and continuum pumping in Lyman lines occur together in an optically thick cloud so that the lines are partially enhanced.
3. This paper is dedicated to understanding line formation processes through Case A, Case B, Case C, and Case D in X-ray-emitting photoionized plasma with Cloudy. We study H- and He-like iron emitting in the X-ray with improved Cloudy energies in excellent agreement with future microcalorimeter observations (Chakraborty et al. 2020a). In our simulations, we use a power-law SED to

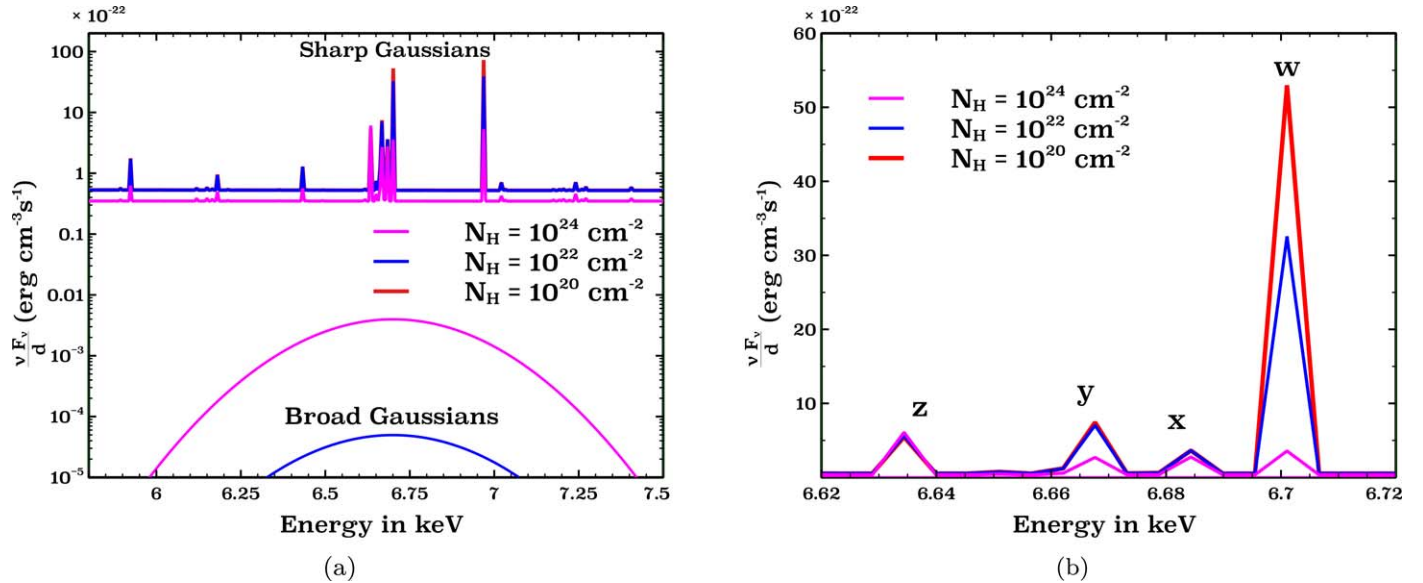


Figure 11. The left panel shows the total scaled emission (sharp line profiles + continuum including the broad line profiles) in log scale at $N_H = 10^{20} \text{ cm}^{-2}$, 10^{22} cm^{-2} , and 10^{24} cm^{-2} in the presence of continuum pumping. The broad Gaussians shown in the figure come from the photons in the Fe XXV K α complex scattered off high-speed electrons and Doppler-shifted from their line-centers. The sharp line profiles come from the originally emitted line photons in the photoionized cloud that are not affected by electron scattering. The $N_H = 10^{24} \text{ cm}^{-2}$ case has significant optical depth for electron scattering, which depresses the continuum. The right panel is a zoomed-in version of the left panel around the Fe XXV K α complex. The emission in w significantly reduces with an increase in column density. The emission in y reduces slightly.

illuminate the cloud and an equilibrium temperature of $6 \times 10^6 \text{ K}$ computed from the heating–cooling balance. Refer to Section 3 for details on the simulation parameters. As the absolute line intensities (I) increase with cloud thickness (d), we compare the line intensities per unit thickness of the cloud (I/d) for estimating the scaled differences between all four cases.

4. Table 1 lists the line intensity (I) per unit thickness (d) of the cloud, I/d , for Case A, Case B, Case C, and Case D conditions observed in nature. To generate optically thin and optically thick conditions in the cloud, the I/d for Cases A and C are computed at $N_H = 10^{19} \text{ cm}^{-2}$, and those for Cases B and D are computed at $N_H = 10^{24} \text{ cm}^{-2}$. The Menzel–Baker Case B values are listed under the Case B_{classic} column in the table. Ly α in H-like iron and K α in He-like iron in Case B_{classic} are enhanced as compared to the corresponding Case A values due to the conversion of higher- n Lyman lines into Ly α (or K α) plus Balmer lines. But in real astronomical sources, the presence of electron scattering reduces the observed Case B values. In H-like iron, I/d for Ly α decreases by $\sim 50\%$. In He-like iron, x , y , and w exhibit a decrease up to $\sim 24\%$. The Case C values are the brightest of all the four cases due to the free escape of Lyman photons following continuum pumping. The Ly α and K α transitions in H- and He-like iron are up to ~ 10 and ~ 27 times enhanced as compared to the corresponding Case A values. The Case D values are smaller than the Case C values but bigger than the Case B values, as they are partially enhanced by continuum pumping. For H-like iron, the Case D I/d for Ly α is $\sim 36\%$ enhanced as compared to the corresponding Case B value. Ly β is $\sim 71\%$ enhanced, and H α is $\sim 36\%$ enhanced. In He-like iron, K α is enhanced up to $\sim 109\%$, K β is enhanced up to $\sim 208\%$, and L α is enhanced up to $\sim 80\%$.
5. The total emission spectrum for Case A, B, C, and D conditions within the energy range 0.1–10 keV is shown in Figure 8. The spectrum includes the continuum

emission as well as the line emission described in the previous paragraphs. The resolving power (R) for our Cloudy simulations is set at $R \sim 1200$, which is the resolving power of XRISM at $\sim 6 \text{ keV}$. The figure shows Case A overplotted with Case C and Case B overplotted with Case D in linear and log scale. Clearly, the line emissions in the Case C spectrum are brighter than those in Case A, and the line emissions in the Case D spectrum are brighter than those in Case B due to continuum pumping and partial continuum pumping, respectively.

6. Electron scattering opacity can play an important role in deciding the line intensities in optically thick clouds. Line intensities for Case B and Case D can be reduced because of this. The top panel of Figure 5 and Table 1 show the deviation of the observed Case B values, which includes the effect of electron scattering, from Case B_{classic}, which does not include electron scattering. The I/d values shown in Table 1 and the bottom panel of Figure 5 for Case D also include electron scattering.
7. Due to the electron scattering opacity, the line photons are scattered off high-speed electrons and are Doppler-shifted from their line-center. These scattered photons form Gaussians with super-broad bases. Line photons that are not scattered have a sharp base equivalent to their thermal width (and turbulent width if turbulence is present). Figure 11 shows these sharp and broad components coming from the Fe XXV K α complex in the presence of continuum pumping for hydrogen column densities $N_H = 10^{20} \text{ cm}^{-2}$, 10^{22} cm^{-2} , and 10^{24} cm^{-2} . $N_H = 10^{20} \text{ cm}^{-2}$ is the Case C limit, and $N_H = 10^{24} \text{ cm}^{-2}$ is the Case D limit. The broad components will be much fainter than the sharp components when detected by high-resolution telescopes. The observed sharp components for the resonance lines will exhibit significant changes in their line fluxes with variation in column density (and optical depth). It can be seen in Figure 11 that the w line intensity decreases significantly with an increase in column density. Such reduction in w is

due to the following two factors: (a) Continuum pumping becomes partially blocked with the increase in optical depth. (b) The large optical depth of w makes it more likely to be scattered by electrons. A combination of (a) and (b) will reduce the line intensity of w or any other resonance line significantly with an increase in column density, which can serve as a powerful diagnostic in measuring the column density/optical depth of the cloud.

From our Cloudy simulation, we get a suppression in w line intensity of ~ 1.43 due to the above two factors at $\tau = 1$, which is as important as the resonance scattering effects described by Gilfanov et al. (1987). As our current Cloudy model assumes a symmetric geometry, the effects of resonance scattering are not included in our calculation. A real observed spectrum will correspond to a resonance-scattering-corrected Cloudy-generated spectrum as shown in this paper.

8. After the discovery of Cases A and B, these two cases have been widely discussed in the literature for the optical, ultraviolet, and infrared regimes, with limited studies on X-rays. As far as we know, there has been no discussion on X-ray spectra under Case C and Case D conditions. Case D is the least discussed of all four cases, as ideally, at very high column densities, Case D should be no different from Case B values, as mentioned in Section 4.4. But Table 1 and the bottom panel of Figure 8 show that even at a column density as high as $N_{\text{H}} = 10^{24} \text{ cm}^{-2}$ in a cloud illuminated with a power-law SED, Case D deviates considerably from Case B for X-ray emission from H- and He-like iron. This deviation will certainly be detected by future high-resolution telescopes with microcalorimeter technology.

We emphasize the fact that Case C and Case D deserve far more attention than they have been given to date, especially because they could be the best representation of the emission spectra from irradiated extragalactic sources with a broad range of column densities.

We thank the referee of this paper for his/her very helpful comments. We thank Stefano Bianchi and Anna Ogorzalek for their valuable comments. We acknowledge support from the National Science Foundation (1816537, 1910687), NASA (17-ATP17-0141, 19-ATP19-0188), and STScI (HST-AR-15018). M. C. also acknowledges support from STScI (HST-AR-14556.001-A).

ORCID iDs

P Chakraborty <https://orcid.org/0000-0002-4469-2518>
 G. J. Ferland <https://orcid.org/0000-0003-4503-6333>
 M. Chatzikos <https://orcid.org/0000-0002-8823-0606>
 F. Guzmán <https://orcid.org/0000-0002-2915-3612>
 Y. Su <https://orcid.org/0000-0002-3886-1258>

References

Baker, J. G., & Menzel, D. H. 1938, *ApJ*, **88**, 52
 Baker, J. G., Menzel, D. H., & Aller, L. H. 1938, *ApJ*, **88**, 422
 Band, D. L., Klein, R. I., Castor, J. I., & Nash, J. K. 1990, *ApJ*, **362**, 90
 Bianchi, S., Miniutti, G., Fabian, A. C., & Iwasawa, K. 2005, *MNRAS*, **360**, 380
 Cappi, M., Panessa, F., Bassani, L., et al. 2006, *A&A*, **446**, 459
 Chakraborty, P., Ferland, G. J., Bianchi, S., & Chatzikos, M. 2020a, *RNAAS*, **4**, 184
 Chakraborty, P., Ferland, G. J., Chatzikos, M., Guzmán, F., & Su, Y. 2020b, *ApJ*, **901**, 68
 Chakraborty, P., Ferland, G. J., Chatzikos, M., Guzmán, F., & Su, Y. 2020c, *ApJ*, **901**, 69
 Chamberlain, J. W. 1953, *ApJ*, **117**, 399
 Ferland, G. J. 1999, *PASP*, **111**, 1524
 Ferland, G. J., Chatzikos, M., Guzmán, F., et al. 2017, *RMxAA*, **53**, 385
 Fukumura, K., & Tsuruta, S. 2004, *ApJ*, **613**, 700
 Gabriel, A. H. 1972, *SSRv*, **13**, 655
 Gilfanov, M. R., Syunyaev, R. A., & Churazov, E. M. 1987, *SvAL*, **13**, 3
 Guainazzi, M., & Bianchi, S. 2007, *MNRAS*, **374**, 1290
 Hanke, M., Wilms, J., Nowak, M. A., et al. 2009, *ApJ*, **690**, 330
 Hitomi Collaboration, Aharonian, F., Akamatsu, H., et al. 2016, *Natur*, **535**, 117
 Hitomi Collaboration, Aharonian, F., Akamatsu, H., et al. 2018a, *PASJ*, **70**, 12
 Hitomi Collaboration, Aharonian, F., Akamatsu, H., et al. 2018b, *PASJ*, **70**, 10
 Hummer, D. G., & Storey, P. J. 1987, *MNRAS*, **224**, 801
 Kallman, T., & Bautista, M. 2001, *ApJS*, **133**, 221
 Kallman, T. R., Palmeri, P., Bautista, M. A., Mendoza, C., & Krolik, J. H. 2004, *ApJS*, **155**, 675
 Keel, W. C., & Windhorst, R. A. 1991, *ApJ*, **383**, 135
 Kelley, R. L., Akamatsu, H., Azzarello, P., et al. 2016, *Proc. SPIE*, **9905**, 99050V
 Kinkhabwala, A., Sako, M., Behar, E., et al. 2002, *ApJ*, **575**, 732
 Koyama, K., Hyodo, Y., Inui, T., et al. 2007, *PASJ*, **59**, S245
 Kramida, A., Ralchenko, Y., Nave, G., & Reader, J. 2018, *APS Division of Atomic, Molecular and Optical Physics Meeting*, **2018**, M01.004
 Liedahl, D. A. 2005, in *AIP Conf. Ser.* **774**, X-ray Diagnostics of Astrophysical Plasmas: Theory, Experiment, and Observation, ed. R. Smith (Melville, NY: AIP), 99
 Luridiana, V., Simón-Díaz, S., Cerviño, M., et al. 2009, *ApJ*, **691**, 1712
 Malkan, M. A., & Sargent, W. L. W. 1982, *ApJ*, **254**, 22
 Mao, J., Kaastra, J. S., Mehdi, M., et al. 2018, *A&A*, **612**, A18
 Mennickent, R. E., Otero, S., & Kołaczkowski, Z. 2016, *MNRAS*, **455**, 1728
 Menzel, D. H. 1937, *ApJ*, **85**, 330
 Menzel, D. H., & Baker, J. G. 1937, *ApJ*, **86**, 70
 Miller, J. M., Fabian, A. C., Wijnands, R., et al. 2002, *ApJ*, **578**, 348
 Osterbrock, D. E., & Ferland, G. J. 2006, *Astrophysics of Gaseous Nebulae and Active Galactic Nuclei* (Sausalito, CA: Univ. Science Books)
 Paerels, F. B. S., & Kahn, S. M. 2003, *ARA&A*, **41**, 291
 Peimbert, A., Peimbert, M., & Luridiana, V. 2016, *RMxAA*, **52**, 419
 Peimbert, M., Peimbert, A., & Delgado-Ingla, G. 2017, *PASP*, **129**, 082001
 Porter, R. L., & Ferland, G. J. 2007, *ApJ*, **664**, 586
 Ross, R. R., Fabian, A. C., & Brandt, W. N. 1996, *MNRAS*, **278**, 1082
 Ross, R. R., Weaver, R., & McCray, R. 1978, *ApJ*, **219**, 292
 Sánchez, S. F., Cardiel, N., Verheijen, M. A. W., et al. 2007, *A&A*, **465**, 207
 Siegbahn, M. 1916, *Natur*, **96**, 676
 Soifer, B. T., Neugebauer, G., Oke, J. B., & Matthews, K. 1981, *ApJ*, **243**, 369
 Stelzer, B., Alcalá, J., Biazzo, K., et al. 2012, *A&A*, **537**, A94
 Storey, P. J., & Hummer, D. G. 1988, *MNRAS*, **231**, 1139
 Storey, P. J., & Hummer, D. G. 1995, *MNRAS*, **272**, 41
 Torrejón, J. M., Schulz, N. S., Nowak, M. A., & Kallman, T. R. 2010, *ApJ*, **715**, 947